PHYSICAL REVIEW B VOLUME 60, NUMBER 2 1 JULY 1999-II

Boron-implantation-induced crystalline-to-amorphous transition in nickel: An experimental assessment of the generalized Lindemann melting criterion

P. C. Liu*
Department of Materials Science & Engineering, Northwestern University, Evanston, Illinois 60208

P. R. Okamoto and N. J. Zaluzec
Materials Science Division, Argonne National Laboratory, Argonne, Illinois 60439

M. Meshii
Department of Materials Science & Engineering, Northwestern University, Evanston, Illinois 60208

(Received 2 February 1999)

The generalized Lindemann melting hypothesis has recently been used to develop a unified thermodynamic criterion for melting applicable to both heat-induced melting and disorder-induced crystalline-to-amorphous (c-a) transformation. The hypothesis stipulates that the sum $\langle \mu^2 \rangle_{\mathrm{Total}}$ of the static and dynamic root-mean-square (rms) atomic displacements is a constant fraction of the nearest-neighbor distance along the melting curve of a solid. To test this hypothesis, energy-filtered selected area electron-diffraction intensity measurements were used to determine the generalized Lindemann parameter $\delta = \sqrt{\langle \mu^2 \rangle_{\mathrm{Total}}}/d_{\mathrm{nn}}$, in which d_{nn} represents the nearest-neighbor distance, as a function of boron concentration during implantation of 50-keV B^+ into polycrystalline Ni at 77 K. The onset of amorphization was found to occur close to 10 at. % boron, which is in good agreement with the value predicted by T_o curve calculated using the generalized Lindemann hypothesis. Moreover, the critical value of the generalized Lindemann parameter for amorphization, $\delta_{\mathrm{Critical}} = 0.115 \pm 0.01$, is within experimental error, identical to that for Ni just below its thermodynamic melting temperature of $T = 1728\,\mathrm{K}$, hence providing a direct confirmation for the generalized Lindemann melting hypothesis. [S0163-1829(99)00326-4]

I. INTRODUCTION

Crystalline-to-amorphous (c-a) transformations have been induced by a variety of solid-state disordering process ranging from energetic particle irradiation, multilayer interdiffusion, hydrogen charging, mechanical alloying, to the application of high pressures.[1,2] Early studies of radiation-induced amorphization of intermetallic compounds[3–5] revealed a number of thermodynamic and kinetic parallels between ordinary melting and disorder-induced amorphization, hinting at the intriguing possibility of a simple melting criterion applicable to both types of phase transformations. However, a major impediment to the development of a unified melting criterion has been the lack of a suitable disorder parameter of sufficient generality that can be used to characterize both heat-induced melting and the ever increasing number of isothermal, damage accumulation processes capable of inducing the c-a transformation. Mechanical instability criteria for the onset of amorphization, based on volume expansion,[5,6] critical strain,[7] or atomic level stress[8,9] as measures of lattice stability, have been proposed. Okamoto, Lam, and Rehn[2] recently pointed out that glass formation ranges predicted by such mechanical instability criteria are not consistent with experimental observations and proposed a simple universal thermodynamic criterion for the onset of heat-induced melting and solid-state amorphization based on the following two hypotheses: (1) The sum of dynamic and static root-mean-square (rms) atomic displacements along the melting curve of a solid is a constant fraction of the nearest-neighbor distance, and (2) all disorder-driven c-a transformations lead to the formation of an ideal glass having the same entropy as the perfect crystal.

The first hypothesis is a generalization of the original Lindemann melting criterion for a perfect crystal[10] that considered only the effects of dynamic, i.e., thermal atomic displacements. The second is a modification of the Kauzmann principle,[11] which stipulates that the entropy of a liquid or glass cannot be less than that of the perfect crystal. Within this conceptual framework, the c-a transformation becomes simply a disorder-driven melting process, albeit one occurring below the glass transition temperature, that leads to the formation of the glassy state with the lowest free energy. The significance of the generalized Lindemann melting hypothesis is that it leads to a generalized polymorphous melting curve (i.e., T_o concept), in which the onset of amorphization (or melting) depends on the magnitude, but not on the physical origin of the rms atomic displacements. Hence, the generalized Lindemann melting criterion should be universal, applicable to isobaric, heat-induced melting as well as to isothermal c-a transformations induced by a wide variety of externally driven, energy dissipative processes. In this paper we report the first direct experimental evidence confirming the generalized Lindemann melting criterion for the onset of amorphization induced by boron implantation into nickel.

II. THERMODYNAMICS OF THE c-a TRANSFORMATION

A. Schematic Gibbs free-energy diagram

The thermodynamics underlying the two hypotheses is illustrated in Fig. 1, which shows schematically the Gibbs free

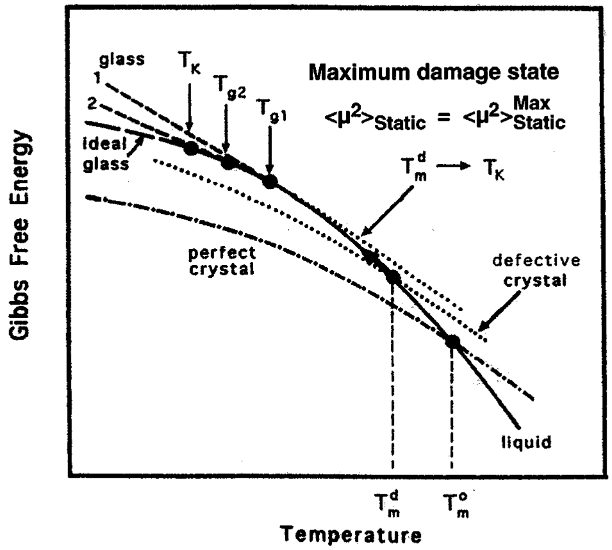

FIG. 1. A schematic Gibbs free-energy diagram showing the relative free-energy change of the various crystal and liquid states with respect to temperature.

energy plotted as a function of temperature for the liquid, the perfect crystal, and two defective crystalline states. Also shown are the free energies of the ideal glass (fully relaxed glass) and two unrelaxed glassy states (1 and 2) having glass transition temperatures $T_K < T_{g2} < T_{g1}$, respectively, with T_K being the ideal glass transition temperature defined using Kauzmann's criterion.[11] The melting temperatures of the perfect and defective crystals, T^o_m and T^d_m, are defined by the intersections of their free-energy curves with that of the liquid phase. Figure 1 shows that melting can occur in two fundamentally different ways. One can melt the crystal by heating it at constant pressure until its free energy becomes equal to that of the liquid at the thermodynamic melting temperature T^o_m. Alternatively, one can also melt the crystal at any fixed temperature $T^d_m < T^o_m$ by introducing enough static atomic disorder such that the Gibbs free energy of the defective crystal becomes equal to that of the supercooled liquid at $T = T^d_m$. The anticipated decrease in the melting temperature T^d_m of a defective crystal with increasing damage level is shown in Fig. 2, in which the static mean-square atomic displacement $\langle \mu^2 \rangle_{\text{Static}}$ has been used as a general measure for the damage level. As the free energy of the defective crystal approaches that of the ideal glass, T^d_m approaches the ideal glass transition temperature T_K, so that the thermodynamic criterion for disorder-induced amorphization becomes $T^d_m \leq T_K$. It follows that the c-a transformation cannot occur for temperatures higher than T_K.

Figure 1 clearly illustrates the thermodynamics underlying the second hypothesis. As the glass with the lowest free energy, the ideal glass will be the glassy state most easily reached from below, that is, from the crystalline state via a disorder-driven c-a transformation, but the most difficult to reach from above, for example, by annealing an unrelaxed glass at temperatures below T_k. Figure 1 also indicates that there is a limit to the amount of damage which can be accumulated in the crystal. This maximum-damage state, $\langle \mu^2 \rangle_{\text{Static}} = \langle \mu^2 \rangle^{\text{Max}}_{\text{Static}}$, occurs when the free energy of a defective crystal becomes tangent to that of the supercooled liquid. Theoretical considerations[12] suggests that the point of tangency occurs at the ideal glass transition temperature, T_K, i.e., when $T^d_m = T_K$ as is assumed in Fig. 2. This point of tangency, denoted by T_K and $\langle \mu^2 \rangle^{\text{Max}}_{\text{Static}}$, defines a critical point at which the first-order melting transformation becomes a second-order (continuous) c-a transition. Since a crystalline state cannot exist for damage levels beyond the maximum-damage state, the melting temperature of the defective crystal T^d_m must drop abruptly at the critical point as shown in Fig. 2. This drop can occur in two different ways: If the free energy curve of the maximum-damaged crystalline state becomes tangent to that of the ideal glass for all temperatures $T < T_K$, then T^d_m will drop vertically at $\langle \mu^2 \rangle_{\text{Static}} = \langle \mu^2 \rangle^{\text{Max}}_{\text{Static}}$. However, if the entropy of the defective crystal at temperatures below T_k exceeds that of the ideal glass, as shown schematically in Fig. 1, then T^d_m in Fig. 2 will follow the dashed line, giving rise to the so-called re-entrant melting curve.[13]

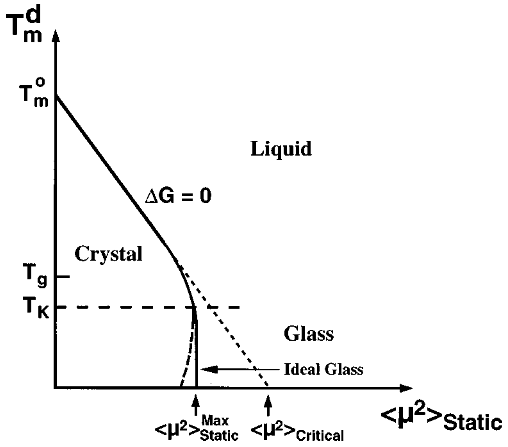

FIG. 2. A generalized polymorphous T_o curve showing schematically the effects of static atomic disorder $\langle \mu^2 \rangle_{\text{Static}}$ on the melting temperature of the defective crystal T^d_m.

B. Generalized polymorphous melting curve

Figure 2 represents a generalized polymorphous melting (T_o) curve for a defective crystal. The T_o curve defines the critical combination of damage level, as measured by $\langle \mu^2 \rangle_{\text{Static}}$, and temperature T at which the Gibbs free energy of the defective crystal is equal to that of the supercooled liquid. It is important to point out that this description of disorder-induced melting is independent of the physical origin of the static mean-square displacement. Hence as a generic measure of static disorder, $\langle \mu^2 \rangle_{\text{Static}}$ can represent the concentration of misfitting solute atoms in an alloy, the amount of Frenkel pairs in a crystal or antisite defects in an ordered intermetallic compound, the average grain size of the nanocrystals or thin films, or any other form of intrinsic or extrinsic defects. For instance, for point defects or misfitting solute atoms in a crystal, $\langle \mu^2 \rangle_{\text{Static}} \propto [x(1-x)]$ where x is the atomic fraction of point defects or solute atoms;[14] for antisite defects in ordered alloys, $\langle \mu^2 \rangle_{\text{Static}} \propto (1-S^2)$ where S is the Bragg-Williams long-range order parameter;[15] and for polycrystalline materials, $\langle \mu^2 \rangle_{\text{Static}} \propto 1/D$ where D is the average grain diameter.[16] It follows that the generalized T_o curve can be used to obtain conventional T_o curves for the binary phase diagrams by expressing $\langle\mu^2\rangle_{\text{Static}}$ as a function of alloy composition.[2,17,18]

III. THE LINDEMANN MODEL FOR SOLID-STATE AMORPHIZATION

In 1910, Lindemann[10] proposed that melting of a defect-free crystal occurs when the root-mean-square amplitude of thermal vibrations of the atoms becomes equal to one-half of the nearest-neighbor distance d_{nn}. This original form of the Lindemann criterion is essentially a mechanical instability criterion since the thermal expansion corresponding to such large thermal displacements would far exceed the critical volume expansion at which a shear modulus vanishes for most metals.[19] The current version of the Lindemann melting criterion, due to Gilvarry,[20] stipulates that thermodynamic melting occurs when the root-mean-square amplitude of thermal vibration, $\langle\mu^2\rangle^{1/2}_{\text{Thermal}}$, reaches a critical fraction δ_{Critical} of the nearest-neighbor distance. Gilvarry's version of the Lindemann melting criterion can be written formally as

$$\langle\mu^2\rangle_{\text{Critical}}=\frac{9\hbar^2T_m^o}{Mk_B\theta_o^2}=\delta^2_{\text{Critical}}d^2_{\text{nn}}, \tag{1a}$$

where T_m^o and θ_o is the thermodynamic melting temperature and Debye temperature of the defect-free crystal, respectively, M is the atomic mass, k_B is Boltzmann's constant, and $\hbar$ is Planck's constant divided by 2π. It follows from Eq. (1a) that

$$T_m^o=\frac{Mk_B\theta_o^2}{9\hbar^2}\langle\mu^2\rangle_{\text{Critical}}. \tag{1b}$$

Okamoto, Lam, and Rehn[2] have pointed out that the c-a transition can be regarded as disorder-induced melting of a defective crystal occurring at temperatures below the ideal glass transition temperature T_k. Melting is assumed to occur when the sum of the thermal and static mean-square atomic displacements attains a critical value identical to that for the onset of thermodynamic melting of the defect-free crystal. This generalized version of the Lindemann melting criterion can be expressed formally by

$$\langle\mu^2\rangle_{\text{Critical}}=\frac{9\hbar^2T_m^d}{Mk_B\theta_d^2}+\langle\mu^2\rangle_{\text{Static}}=\delta^2_{\text{Critical}}d^2_{\text{nn}}, \tag{2}$$

where T_m^d is the melting temperature of the defective crystal and $\langle\mu^2\rangle_{\text{Static}}$ is the static component of the total mean-square atomic displacement associated with defects in the crystal.

The linear region of the generalized polymorphous melting curve in Fig. 2 is, in fact, a graphical statement of the generalized Lindemann melting criterion (GLMC). This follows from Eq. (2), which can be rewritten in a form identical to Eq. (1b), i.e.,

$$T_m^d=\frac{Mk_B\theta_d^2}{9\hbar^2}\langle\mu^2\rangle_{\text{Critical}} \tag{3a}$$

with a disorder-dependent Debye temperature θ_d^2 given by

$$\theta_d^2=\theta_o^2\left[1-\frac{\langle\mu^2\rangle_{\text{Static}}}{\langle\mu^2\rangle_{\text{Critical}}}\right]. \tag{3b}$$

Equation (3a) shows that the linear decrease in melting temperature with increasing $\langle\mu^2\rangle_{\text{Static}}$, shown in Fig. 2, simply reflects the effect of static atomic disorder on the Debye temperature described by Eq. (3b). Since θ_d^2 for an elastically isotropic solid scales linearly with the average shear modulus G_d,[21] the linear decrease in melting temperature should be directly observable as a disorder-induced softening of the average shear modulus having the same functional dependence on $\langle\mu^2\rangle_{\text{Static}}$ as Eq. (3b). Hence a direct corollary of the GLMC is that the reduced quantities T_m^d/T_m^o, θ_d^2/θ_o^2, and G_d/G_o all must be equal and have the same functional dependence on $\langle\mu^2\rangle_{\text{Static}}$, i.e.,

$$\frac{T_m^d}{T_m^o}=\frac{\theta_d^2}{\theta_o^2}=\frac{G_d}{G_o}=\left[1-\frac{\langle\mu^2\rangle_{\text{Static}}}{\langle\mu^2\rangle_{\text{Critical}}}\right]. \tag{4}$$

Equation (4) shows that the GLMC is a "law of corresponding states,"[22] depicting a scaling relationship which correlates the changes in the physical properties of the crystal to a universal disorder parameter that characterize the state of the disorder relative to a reference state. Within the framework of GLMC the dimensionless Lindemann parameter, $\delta=\sqrt{\langle\mu^2\rangle_{\text{Total}}}/d_{\text{nn}}$, serves as a universal disorder parameter for both disorder-induced c-a transformations and ordinary melting. Hence, a critical test of the GLMC for c-a transitions would be to show that the critical value δ_{Critical} for the onset of the amorphization is the same as that for the onset of the melting. Although values for δ for the melting case are available for many metals,[20,22–26] corresponding values of δ_{Critical} for the onset of amorphization have not been determined for any metal.

In this paper, we report the first measurements of δ_{Critical} and the corresponding critical boron concentration associated with the onset of amorphization of Ni-B solid solution during implantation of Ni with 50-keV B^+ ions. Energy-filtered selected-area electron diffraction (EFSAED) (Ref. 27) was used to determine $\langle\mu^2\rangle_{\text{Total}}$ from Debye-Waller factors[28] extracted from measured changes in the crystalline peaks intensities caused by the implantation process. Within the framework of the GLMC, the thermodynamic criterion for the onset of amorphization is $T_m^d=T_K$. Hence if the GLMC is correct, the critical boron concentration C^* for the onset of amorphization of Ni-B solid solution will be given by the intersection of the T_o and the T_k curves, expressed as a function of B concentration on the Ni-B binary phase diagram. The generalized form of the conventional T_o curve derived from Eq. (4) is given by

$$T_m^d=T_m^o\left[1-\frac{\langle\mu^2\rangle_{\text{Static}}}{\langle\mu^2\rangle_{\text{Critical}}}\right]. \tag{5}$$

While it is not possible to achieve polymorphous melting directly by heating, measurement of $\langle\mu^2\rangle_{\text{Static}}$ as a function of implanted B concentration would allow the construction of the T_o curve for the Ni-B binary system using Eq. (5).

IV. EXPERIMENT

Quantitative comparison of energy-filtered selected-area electron diffraction (EFSAED) intensity measurements between crystalline and amorphous phases requires thin randomly oriented polycrystalline thin films as the starting target. Nontextured thin Ni films were prepared by evaporating 99.99% purity Ni onto commercial Bioden™ R.F.A. acetyl cellulose film substrates held at room temperature in a vacuum of 3×10^{-7} Torr. The deposited films were subsequently dissolved in acetone to obtain Ni films supported on Cu grids. The thickness of the deposited Ni films, determined by the Rutherford-backscattering (RBS) technique, was 650 Å. Electron-diffraction patterns and bright-field (BF) images obtained using transmission electron microscopy (TEM) showed that the thin-film morphology consisted of a nontextured polycrystalline fine-grain structure with an average grain size of 17 ± 5 nm. The average lattice constant for the film, obtained by selected-area electron diffraction (SAED), is 3.53 Å, as compared to the bulk Ni value of 3.5238 Å determined by x-ray diffraction.[29]

Ex situ ion implantation experiments were performed at the Argonne National Laboratory's HVEM/Tandem accelerator facility using 50-keV B^+ ions directed at normal incidence to the Ni film. TRIM calculations,[30] based on a modified Kinchin-Pease model, indicate that 50-keV B^+ ions would be distributed uniformly over a thickness of about 400 Å centered on the peak implant depth of 830 Å. To produce a more uniform implantation profile over a wider thickness range, and to minimize sputtering effects, an energy degrader consisting of 650-Å-thick polycrystalline Ni thin film supported on 100-mesh Cu grids was placed in front of the target Ni films of the same thickness supported on 300-mesh Cu grids. Both the target and degrader films were kept at ~77 K during implantation using a liquid-nitrogen cold stage. *In situ* monitoring of the specimen temperature by Ircon™ infrared pyrometry showed that beam heating of the Ni films was less than the minimum detection limit of 100 °C.

TEM specimens with implant doses from 0.4–$4.0\times10^{17}B^+/cm^2$ were produced. Thickness measurements[31] using parallel electron energy-loss spectrometer (PEELS) showed that there were no significant changes to the target film thickness during implantation, suggesting that the sputtering of the target film has been sufficiently compensated by the additional thickness increase due to the addition of boron solutes and radiation damages. The nuclear reaction $^{11}B(p,\alpha)2\alpha$ technique of Vollmer *et al.*[32] was used to calibrate the actual amount of B^+ ions implanted in the Ni target films. The yield of α particles emitted from the nuclear reaction of 700-keV incident protons with the ^{11}B nucleus (80.2% natural abundance) was calibrated against boron standards to provide the boron atomic concentration as a function of incident B^+ implantation dose. The resulting calibration curve shown in Fig. 3 indicates that boron concentrations measured are within the saturation limit and hence provides a direct measure of the Ni-B composition in the target film for a given incident B^+ implantation dose.

Microstructural characterization of the B^+ implanted Ni films was carried out using a Philips EM420 TEM equipped with a serial electron energy-loss spectrometer (Gatan Model 607) operating at 100 kV.[27,33] Two-dimensional EFSAED patterns were acquired by computer-controlled scanning (EDAX 9900) of SAED patterns across the entrance aperture of the serial EELS which records the intensities via a photomultiplier tube. The spectrometer energy window was adjusted to a width of 5~6 eV centered on the elastic peak of the energy-loss spectrum. The electron beam probe used to acquire EFSAED patterns covered a circular area of 154.5 mm in diameter at a nominal magnification of 18.5 k× in the bright-field (BF) mode. The 100-mesh Cu grids supporting the Ni energy degrader foil shadowed regions of the final target film, thus providing both unimplanted and implanted regions on the same sample. With this configuration, the effect of sample-to-sample variation in EFSAED measurements is minimized by a direct comparison of the implanted and the unimplanted (control) regions on the same sample.

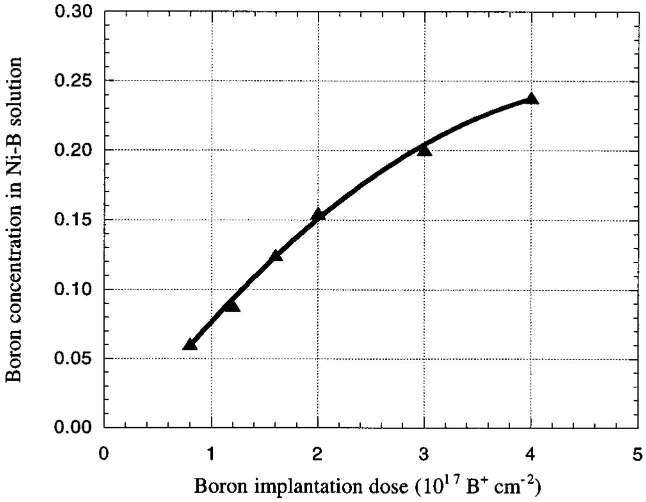

FIG. 3. Empirically assessed boron concentration in the Ni target film as a function of incident B^+ implantation dose; Ni-B composition determined using nuclear reaction of $^{11}B(p,\alpha)$ with 700 keV protons and 170° detector angle.

V. RESULTS

A. General morphology

The implantation-induced c-a transformation process was monitored by TEM imaging (Fig. 4) and EFSAED measurement (Fig. 5). BF [and dark-field (DF)] images showed that little or no grain growth occurs during implantation, and that the c-a transition proceeds via preferential amorphization of high-energy regions (e.g., grain boundaries and grain-boundary junctions) followed by subsequent growth of the amorphous phase into surrounding crystalline matrix. The disappearance of smaller grains at low implantation doses, the smearing of grain-boundary contrast, and the diminution of remaining larger grains when encroached by the surrounding amorphous phase, all indicate that amorphization proceeds heterogeneously. EFSAED intensity profiles shown in Fig. 5 suggests that the c-a transformation, as evidenced by the appearance of weak intensity halos near the (111) and (220) Bragg peaks, begins at a dose of about $0.7\times10^{17}B^+/cm^2$ which corresponds to 5 at. % boron concentration. With increasing dose the diffuse intensity halos become more pronounced at the expense of the fcc crystalline

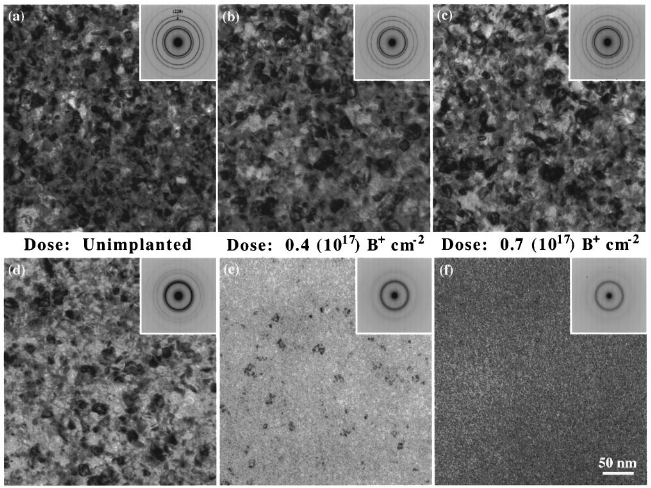

FIG. 4. TEM BF images and the corresponding SAED patterns showing the morphological change accompanying the B^+-implantation-induced amorphization in Ni crystals.

peaks. Complete amorphization of the film, defined as the state at which all Bragg peaks disappear in the SAED pattern, occurs at about $2.0\times10^{17}\,B^+/cm^2$, corresponding to 15 at. % boron, and to a TRIM calculated ion damage level of 31 dpa (displacement per atom). The experimentally determined boron concentrations for both the initiation and the completion of the c-a transformation are in good agreement with the RBS channeling results of Drigo *et al.*[34] who investigated the kinetics of 50-keV boron-implantation-induced amorphization of Ni single crystals at liquid-N_2 temperature.

B. Microstructural studies

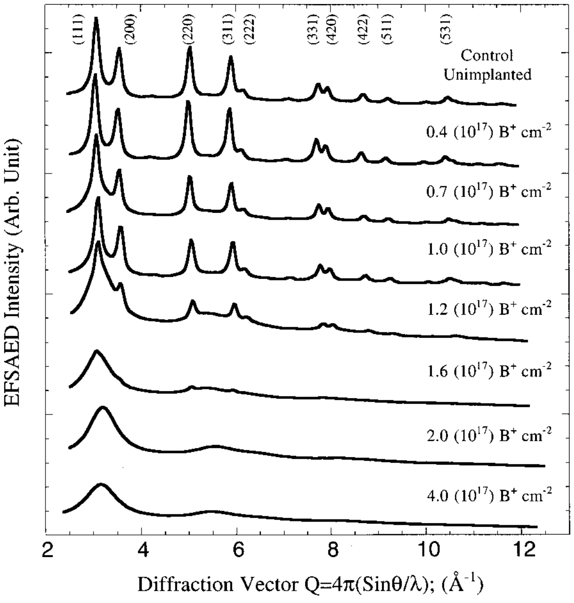

FIG. 5. EFSAED intensity profiles as a function of B^+ implantation dose, with the initiation and the completion of the c-a transformation occurred at 0.7 and $2.0\times10^{17}\,B^+/cm^2$, respectively.

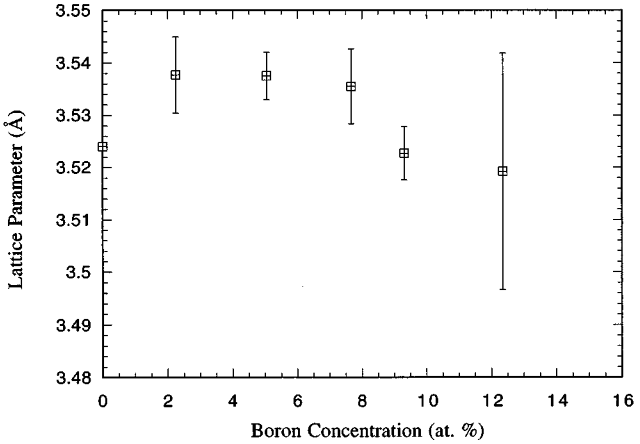

FIG. 6. The change in the lattice parameter of Ni-B solid solution as a function of implanted boron concentration determined from SAED measurements.

Because the c-a transition proceeded via a nucleation and growth process, it is important to determine the volume fractions of the crystalline and amorphous phases present in the implanted region as a function of incident B^+ dose. For this purpose dark-field (DF) imaging and integrated SAED intensity normalization techniques were employed to measure the volume fraction of the crystalline phase. Both methods exploit the fact that the amount of crystalline phase present in the implanted region is reflected in the total integrated intensity of its fcc polycrystal rings. In the DF method, the area fraction of the crystalline grains illuminated using DF imaging of a portion of the polycrystalline ring from the implanted region, normalized to that of the corresponding control region imaged with the same part of the polycrystalline ring, gives a measure of the volume fraction of the remaining crystalline phase. An alternative means for determining the relative change in crystalline phase volume fraction is to normalize the integrated Bragg peak intensity of the implanted region to the corresponding peak intensity of the control region. Selected portions of the (220) ring were used for static DF imaging, mainly because of its prominent intensity and distinct separation from diffuse intensity halos. The (111), (200), (220), and (311) reflections were used for integrated SAED peak intensity normalization. Since no extraneous diffraction peaks appeared during implantation, the phase distribution in the implanted region is taken as a simple summation of crystalline (f_c) and amorphous (f_a) phase volume fractions, so that f_a is simply given by $f_a=1-f_c$.

Changes in the lattice parameter of the crystalline Ni-B solid solution as a function of B concentration were also determined using an Al thin film calibration standard. The results in Figure 6 show that the lattice parameter initially increases by about 0.4%, reaches a flat maximum centered on 5 at. % boron, then decreases with further B^+ implantation. In Fig. 7 the crystalline volume fraction obtained from both DF imaging and normalized SAED intensities was plotted as a function of final Ni-B composition. Also shown is the crystalline volume fraction data obtained during the extraction of Debye-Waller parameter (DWP) from the modified Wilson plots. Linker[35] has shown that the DWP approach can be used to extract changes in the crystalline volume fractions via the relative changes in the ''intensity scaling factor''for the respective SAED spectrum, the magnitude of which depends on the amount of crystalline grains giving rise to the Bragg reflections. The sharp drop in the crystalline volume fraction at around 5 at. % B, where the

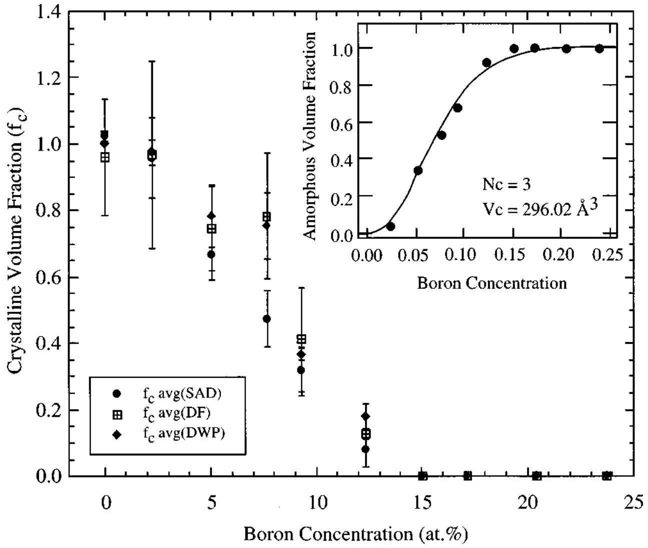

FIG. 7. The progression of the remaining crystalline volume fraction f_c as a function of implanted boron concentration. Three different techniques were employed: SAD for selected-area electron diffraction, DF for dark-field imaging, and DWP for modified Wilson plots. The amorphous volume fraction is taken as $f_a = 1 - f_c$ based on SAD measurements which exhibits the most consistent trend. The inset shows the fitting results based on Drigo *et al.*'s statistical approach for modeling the kinetic of ion-implantation-induced c-a transformation (Ref. 34).

lattice parameter reaches a maximum, suggests that the initiation of the c-a transformation and the maximum in lattice parameter are correlated, an observation also reported by Linker in his studies of boron-implantation-induced amorphization of niobium and molybdenum films.[35,36]

C. Comparison with kinetic models of amorphization

Drigo *et al.*[34] have proposed a statistical model for the kinetics of ion-implantation-induced amorphization, in which the minimum cluster size (V_c) and the critical solute concentration for the formation of amorphous clusters (C_c), can be extracted from the concentration dependence of the amorphous phase volume fraction during the c-a transition process. In this model the region at the implantation depth is subdivided into small identical volume elements V_c, and amorphization is assumed to occur when the number of B atoms in a cluster is at least N_c with the mean number of B atoms in the volume V_c equals to $\overline{N}$. The amorphous volume fraction f_a for any average B concentration C_B will then be given by:

$$f_a = \sum_{N=N_c}^{\infty} (\overline{N})^N \exp(-\overline{N})/N!. \tag{6}$$

In arriving at the above expression the probability distribution of N (actual number of B atoms in the volume V_c) around the mean value $\overline{N}$ is assumed to be given by Poisson statistics. The mean number $\overline{N}$ of B atoms in a cluster is proportional to the elementary volume V_c and to the average concentration C_B of B in the sample. Labeling C_c the critical average B concentration corresponding to N_c, the experimental curve, $f_a = 1 - f_c$, can be fitted to Eq. (6) by varying the parameters V_c and C_c as shown in the inset of Fig. 7. The best-fit values of the minimum cluster size V_c and the critical average concentration C_c in the amorphous clusters for the current experiment were determined to be $4.52 \times 10^{-22}\,\mathrm{cm}^3$ and 8.7 at. %, respectively. These values are in reasonably good agreement with the single-crystal channeling results of Drigo *et al.*, who obtained $V_c = 15 \times 10^{-22}\,\mathrm{cm}^3$ and $C_c = 9.3$ at. % for the Ni-B system.[34] We believe our smaller value for V_c is due to the abundance of grain boundaries in the polycrystal TEM specimen, which provides more nucleation sites for amorphous cluster formation than does the single-crystal channeling specimen.

D. Inelastic and multiple-scattering effects

For electron diffraction, inelastic and multiple-scattering effects must be considered in any quantitative analysis of diffraction intensities.[37] The problem of inelastic scattering, a major source of uncertainty in the extraction of structural parameters from electron-diffraction intensities, has been addressed in this study by employing an energy filter to remove most of the inelastically scattered intensity. The use of analog and digital signal processing equipment to record the electron intensity directed into the photomultiplier tube also avoided any nonlinear effects associated with microdensitometry measurements on the photographic SAED negatives.

The more difficult problem of multiple (plural) scattering can be minimized by using high-energy electrons and very thin samples. Blackman[38] proposed the following criterion for the critical thickness denoting the transition from kinematic to the dynamic scattering regimes: $\lambda|\Phi_{hkl}/\Omega|A_3' \approx \pi/2$, where λ is the incident electron wavelength, Φ_{hkl} is the structural amplitude of the reflection denoted by Miller indices *hkl*, Ω is the volume of the unit cell, and A_3' is the critical thickness for the transition into the dynamical scattering regime. A more conservative criterion proposed by Vainshtein[39] is $\lambda|\Phi_{hkl}/\Omega|A_3' \approx 1$. The critical thickness data obtained using Blackman's and Vainshtein's criteria for 100 keV incident electrons into Ni, tabulated in Table I, indicate that for 650-Å-thick Ni thin films used in our experiments, the kinematic approximation for the diffraction intensity would be justified only at large scattering angles. To correct for the multiple-scattering effect in the low-Q range, where $Q = 4\pi \sin\theta/\lambda$, a correction method proposed by Gjønnes[40] was used to extract the single-scattering intensity from the experimental electron-diffraction curves. In this method the multiple-scattered intensity is considered as a convolution of single-scattered intensities from a number of layers proportional to the number of effective "single-scattering layers" within the specimen thickness. Employing the PEELS thickness measurement together with the elastic mean free path estimated from the relative magnitudes of electron interaction cross sections, single-scattered intensities were deconvoluted using the Hankel transform technique.[41,42] The resulting diffraction intensity pattern exhibits relative Bragg peak intensities in the lower Q ranges which are comparable to the single-scattered intensity calculated using the kinematical approximations.

E. Mean-square atomic displacement

If the instantaneous position vector of an atom n is $r_n(t)$ and its equilibrium lattice position is r_n^o, then the mean-

TABLE I. The critical thickness data for 100-keV electron diffraction in Ni thin films (650 Å thick) computed using Blackman's and Vainshtein's criterion. Noted that the value of critical thickness A'_3, which denotes the transition from the kinematic to the dynamic scattering regimes, increases for higher order Bragg reflections.

Ni's Bragg reflections	(111)	(200)	(220)	(311)	(222)	(400)	(331)	(420)	(422)	(511)	(333)	(440)	(531)	(600)	(442)
A'_3 (Å) Blackman	151	171	247	300	318	387	438	454	521	570	570	651	700	716	716
A'_3 (Å) Vainshtein	96	109	157	191	202	246	279	289	331	363	363	415	445	456	456

square atomic displacement (MSD) is defined as the square of the difference between these two position vectors averaged over an ensemble of all n atoms:[43]

$$\langle \mu^2 \rangle_{\text{Total}} \equiv \langle (r_n(t) - r_n^o)^2 \rangle. \tag{7}$$

The effect of thermal vibrations of atoms on the intensity of crystalline reflections is given by the Debye-Waller temperature factor $\exp[-2M]$.[28] Assuming that the static atomic displacement follows a Gaussian distribution, the total MSD $\langle \mu^2 \rangle_{\text{Total}}$ determined from the experimental Debye-Waller factor will be the sum of the thermal and static MSD components. Strictly speaking, if a crystal contains more than one kind of atom, there will be a separate M_n factor for each atomic species n given by the expression[28]

$$M_n = 8\pi^2 \langle \mu^2 \rangle_n \sin^2 \theta / \lambda^2, \tag{8}$$

where $\langle \mu^2 \rangle_n$ is the MSD component along the direction normal to the planes of reflection (for an isotropic material the total MSD is three times $\langle \mu^2 \rangle_n$). However, for our experiment we have obtained an averaged value M_{Avg} because molecular dynamic simulations of defect-induced c-a transformations in complex crystalline compounds have shown that it is the average mean-square atomic displacement which must be used in the applications of the generalized Lindemann melting criterion.[44]

Two methods are generally used to extract the Debye-Waller temperature factor from integrated peak intensities: Warren's method,[28] which yields the absolute value of the Debye-Waller parameter, and James' method,[45] which gives the relative change in the Debye-Waller parameter relative to some reference state. In Warren's method, the sample is assumed to be free of texture and the reduction in the integrated peak intensity with diffraction wave vector is given by

$$\ln\left(\frac{1000 I_{hkl}}{F_{hkl}^2 m_{hkl}}\right) = \ln(K) - 2B \frac{\sin^2 \theta}{\lambda^2}, \tag{9}$$

where I_{hkl} is the integrated intensity of the hkl reflection, F_{hkl}^2 and m_{hkl} are, respectively, the square of the structure factor amplitude and the multiplicity factor for the hkl reflection, K is a constant which scales with the incident intensity and diffracting volume, and the last term $-2B \sin^2 \theta/\lambda^2$ comes from the Debye-Waller factor $\exp[-2M]$ in which the total MSD is related to the factor B by the relation $B = (8\pi^2/3)\langle \mu^2 \rangle_{\text{Total}}$. For polycrystalline samples with preferred orientation, James' method can be used to avoid the texture problem by taking the ratio of Eq. (9) for successive damaged states relative to a reference state (assuming that texture remains unchanged):

$$\ln\left(\frac{I_{\text{Implant}}}{I_{\text{Control}}}\right) = \ln\left(\frac{K_{\text{Implant}}}{K_{\text{Control}}}\right) - 2(B_{\text{Implant}} - B_{\text{Control}}) \frac{\sin^2 \theta}{\lambda^2}. \tag{10}$$

It is clear that from Eq. (10) that a linear fit of $\ln(I_{\text{Implant}}/I_{\text{Control}})$ with $\sin^2 \theta/\lambda^2$ (using the modified Wilson plot) would give the difference between the Debye-Waller parameters for the implanted region relative to the reference (unimplanted) region of the same sample. Since all EFSAED experiments were performed under similar illumination condition with approximately the same incident intensity, the ratio $(K_{\text{Implant}}/K_{\text{Control}})$ derived from the y intercept would represent the reduction in crystalline volumes giving rise to the Bragg reflections, thus providing an additional measure of the change in crystalline volume fraction with B^+ implantation dose.

Using single-scattered intensity profiles extracted via the Hankel transform technique, peak intensity information for each Bragg reflection have been obtained by performing a simultaneous fitting of multiple Lorentian peak profiles superimposed on a third-order polynomial background fit. Figure 8 shows the modified Wilson plots for each implantation dose. These plots show that $\langle \mu^2 \rangle_{\text{Total}}$, represented by the linear slope fit in accordance with Eq. (9), increases as more boron is implanted into nickel. Figure 9 shows the variation of $\langle \mu^2 \rangle_{\text{Total}}$ as a function of implanted boron concentration obtained by combining the averaged results of Warren and James methods. The average absolute value for all the initial reference states (i.e., all control samples), is $\langle \mu^2 \rangle_{\text{Total}} = 0.039\,\text{Å}^2$. This value for $\langle \mu^2 \rangle_{\text{Total}}$ is significantly larger than the range of 0.010–0.016 Å^2 derived from the specific-heat measurements of bulk Ni crystals at 293 K.[46] The larger initial value of $\langle \mu^2 \rangle_{\text{Total}}$ for our thin-film samples relative to the bulk samples may be due to the combination of much finer grain size, greater surface-to-volume ratio, and the high concentration of nonequilibrium defects typically produced by the vapor deposition process. Figure 9 shows that $\langle \mu^2 \rangle_{\text{Total}}$ increases very slowly up to a dose of $1.0 \times 10^{17}\,\text{B}^+/\text{cm}^2$ (7.7 at.% boron). From there it rises sharply to a value of 0.083 Å^2 at a dose of $1.6 \times 10^{17}\text{B}^+/\text{cm}^2$ (12.4 at.% boron), where the last observable remnants of the crystalline phase contributed to the peak intensities. Hence $\langle \mu^2 \rangle_{\text{Total}} = 0.083\,\text{Å}^2$ is taken as the value of the MSD in the crystalline phase just prior to the onset of amorphization, i.e., the critical value for melting as defined

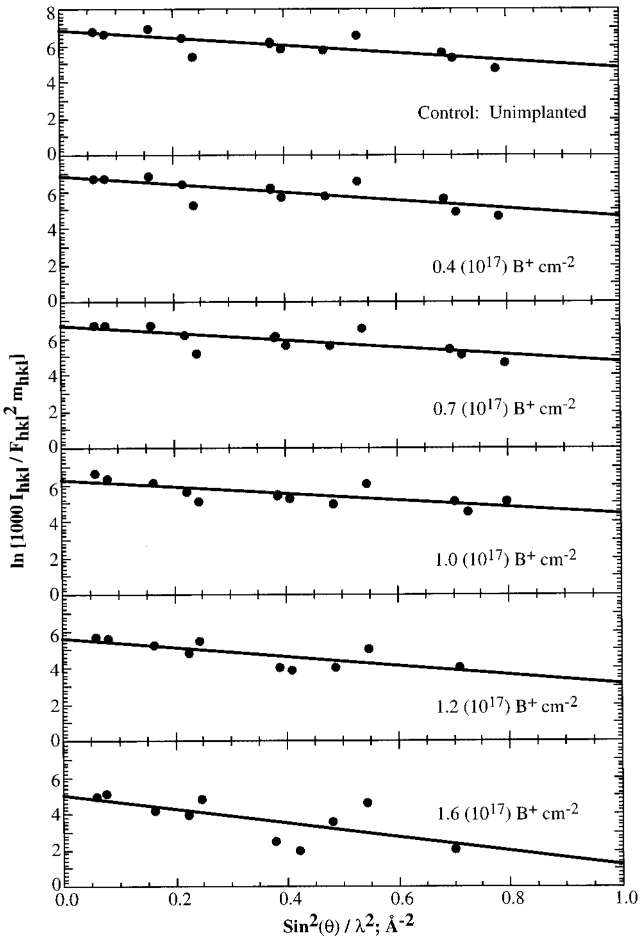

FIG. 8. The modified Wilson plots for each B^+ implantation dose plotted in accordance with Eq. (9). The values of linear slope fits progressively steepens as more B^+ were implanted into Ni, indicating a corresponding increase in $\langle\mu^2\rangle_{\text{Total}}$.

by the GLMC. The corresponding value of the nearest-neighbor distance based on the lattice parameter measured at this dose is 2.50 Å. Consequently the critical value of the Lindemann parameter for the onset of implantation-induced amorphization is $\delta_{\text{Critical}}=\sqrt{\langle\mu^2\rangle_{\text{Critical}}}/d_{\text{nn}}=0.115\pm0.01$, with the experimental error range given by the standard deviation of two independent measurements.

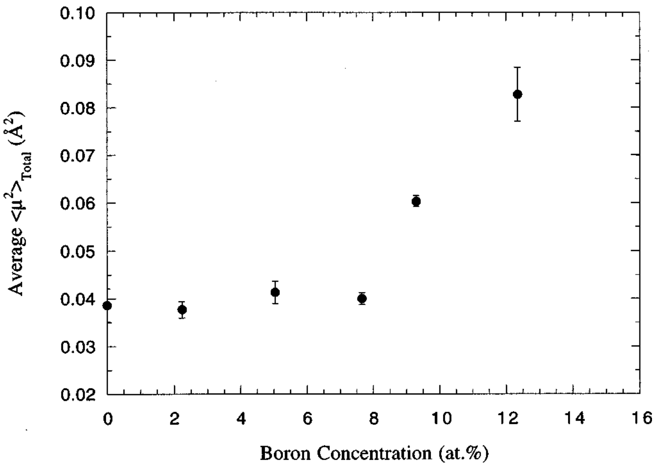

FIG. 9. The variation of $\langle\mu^2\rangle_{\text{Total}}$ as a function of implanted boron concentration. The absolute magnitude of $\langle\mu^2\rangle_{\text{Total}}$ is taken as the sum of the average $\langle\mu^2\rangle_{\text{Total}}$ for the initial reference state (0.039 Å^2) plus the corresponding change in the relative magnitude obtained for each successive implantation dose using James' method.

VI. VERIFICATION OF THE GENERALIZED LINDEMANN MELTING HYPOTHESIS

A. Experimental assessment of the critical Lindemann parameter

The GLMC assumes that the critical Lindemann parameter δ_{Critical} for a crystal at the onset of disorder-induced amorphization is identical to that for ordinary heat-induced melting. This hypothesis rests on the implicit assumption that the defect structure introduced by the disordering process is effectively frozen. The process of implanting B atoms into Ni polycrystalline thin films at liquid-nitrogen temperature constituted an effective way of producing a high supersaturation of "permanent" defects in Ni in the form of misfitting solute atoms without inducing precipitation of equilibrium phases. The critical Lindemann parameter δ_{Critical} for the onset of amorphization determined from the implantation experiment is listed in Table II, along with values of δ_{Critical} reported for heat-induced melting in Ni and other selected fcc elements. All the δ_{Critical} values reported in Table II for melting are either theoretical values or experimental values determined indirectly from elastic constant measurements. The scarcity of empirical-based values for δ_{Critical} for ordi-

TABLE II. Tabulation of the critical Lindermann parameter δ_{Critical} for the onset of solid-state amorphization (from this experiment) and those reported for melting of Ni and other selected fcc elements obtained using theoretical calculations.

Selected fcc elements	$T_m^{0\,a}$ (K)	Lattice parameter at 298 K^a (Å)	δ_{Critical} amorphization ion implantation	δ_{Critical} melting^b Cho (adjusted)	δ_{Critical} melting^c Shapiro	δ_{Critical} melting^d Gupta *et al.*	δ_{Critical} melting^e Singh *et al.*	δ_{Critical} melting^f Gilvarry	δ_{Critical} melting^g Cartz
Al	933	4.05		0.0566	0.072	0.1082	0.1044	0.0664	0.1102
Ni	1728	3.524	0.115±0.01	0.0576 (0.080)	0.077	0.0933	0.0959	0.0847	0.1144
Cu	1356	3.616		0.0598	0.069	0.1077	0.1054	0.0792	0.1182
Au	1336	4.07		0.0590	0.075	0.0922	0.1054		0.1089

[a] Reference 47.
[b] Reference 23.
[c] Reference 24.
[d] Reference 25.
[e] Reference 26.
[f] Reference 20.
[g] Reference 22.

nary melting is due mainly to the difficulties involved in making accurate scattering measurements at such high temperatures. The δ_{Critical} values reported by Singh and Sharma (1968),[26] Gupta and Sharma (1968),[25] and Shapiro (1970) (Ref. 24) were calculated from lattice dynamics based on the treatment of the frequency spectrum analyses. The δ_{Critical} values of Cartz (1955)[22] and Gilvarry (1956)[20] were obtained by performing analyses using the Debye-Waller theory. More recently Cho (1982)[23] derived an analytical Lindemann fusion relationship based on a combination of the atomic model of the lattices and the simple theory of harmonic vibration of atoms in the crystal. The large difference between Cho's values and the others in Table II is due mainly to his definition of the critical Lindemann parameter, $\delta_{\text{Critical}} = \sqrt{\langle\mu^2\rangle_{\text{Critical}}}/(d_{nn}^{\text{w-s}}/2)$, which normalizes the root-mean-square amplitude of the atomic vibrations with respect to $\frac{1}{2}$ of the nearest-neighbor distance $d_{\text{nn}}^{\text{w-s}}$, with $d_{\text{nn}}^{\text{w-s}}$ defined using Wigner-Seitz cellular method. If Cho's maximum vibrational amplitude for Ni at fusion, $\langle\mu^2\rangle_{\text{Critical}}^{1/2} = 0.2030\,\text{Å}$, is normalized to the conventional nearest-neighbor distance d_{nn} as determined from thermal expansion data $[d_{\text{nn}}(\text{Ni}) = 2.55\,\text{Å}$ at $T_f = 1728\,\text{K}]$,[47] the resulting value, $\delta_{\text{Critical}} = 0.08$, is in much better agreement with other values reported for Ni. The δ_{Critical} values reported by Cartz, including the one for Ni, are significantly larger than all the others because he used room-temperature values of lattice constant and Debye temperature in his evaluation. In this respect, Gilvarry's values are probably more accurate than Cartz's since he evaluated the critical Lindemann parameter using the physical and thermodynamic properties at the fusion point $T_f = 1728\,\text{K}$. Robbins, Grest, and Kremer (1990) pointed out that the effect of finite system size used for lattice-dynamics calculations and molecular-dynamics simulations tends to underestimate the magnitude of MSD by about 10~20% for system sizes ranging from 500~1000 particles.[48] Correcting for this effect would make δ_{Critical} for heat-induced melting of Ni crystal averaged over all reported values equal to 0.095 ± 0.013, which is about 20% smaller than the experimentally measured δ_{Critical} value of 0.115 ± 0.01 for B^+ implantation-induced amorphization in Ni.

The discrepancy between the critical value of the Lindemann parameter determined empirically for amorphization and the theoretically derived values for melting is mostly due to the use of simple harmonic approximation for $\langle\mu^2\rangle_{\text{Thermal}}$ employed in the theoretical calculations. For a harmonic Debye solid the temperature dependence of $\langle\mu^2\rangle_{\text{Thermal}}$ is given by[43]

$$\langle\mu^2\rangle_{\text{Thermal}} = \frac{9\hbar^2 T}{M k_B \theta_o^2}[\Phi(\theta_o/T) + 1/4(\theta_o/T)], \tag{11a}$$

where Φ is the Debye integral function:

$$\Phi(x) = \frac{1}{x}\int_o^x \frac{z}{e^z - 1}\,dz; \quad \Phi(x) = 1 - \left(\frac{x}{4}\right) + \left(\frac{x^2}{36}\right) - \cdots \quad (\text{for small } x). \tag{11b}$$

At high temperatures $(T \gg \theta_o)$ the integral factor $[\Phi(\theta_o/T) + 1/4(\theta_o/T)]$ in Eq. (11a) can be neglected, leading to the linear relationship between $\langle\mu^2\rangle_{\text{Thermal}}$ and temperature given by Eq. (1a), the form used in most evaluations of δ_{Critical} for the fusion point. Equation (11a) can be compared with Fig. 10, which shows experimental values of $\langle\mu^2\rangle_{\text{Thermal}}$ obtained by x-ray diffraction measurement for temperatures up to ~800 K.[49,50] Assuming a direct proportionality between $\langle\mu^2\rangle_{\text{Thermal}}$ and temperature T(K), linear extrapolations based on Simerská's (1962) (Ref. 49) and Wilson, Skelton, and Katz's data (1966) (Ref. 50) for temperatures up to $\sim\frac{1}{2}\,T_m^o$ of Ni give $\langle\mu^2\rangle_{\text{Thermal}} = 0.081\,\text{Å}^2$ and $0.105\,\text{Å}^2$ at $T_m^o = 1728\,\text{K}$, respectively. Indeed by using the Debye temperature of $\theta_o = 390\,\text{K}$ for pure Ni, Eq. (11a) gives an excellent fit to the low-temperature values of $\langle\mu^2\rangle_{\text{Thermal}}$. However, the increasing departure of $\langle\mu^2\rangle_{\text{Thermal}}$ from a linear temperature dependence indicates the increasing importance of anharmonic effects on the vibrational amplitude of atoms as the crystal approaches its melting point. To obtain an estimate for $\langle\mu^2\rangle_{\text{Thermal}}$ at T_m^o, a second-order polynomial fit to the low-temperature data up to 800 K was used to extrapolate the curve to the melting point. This procedure yields a value of $\langle\mu^2\rangle_{\text{Thermal}} = 0.145\,\text{Å}^2$ as compared to $\langle\mu^2\rangle_{\text{Thermal}} = 0.085\,\text{Å}^2$ obtained using the simple harmonic Debye model. Extrapolation of the experimental temperature dependence of lattice spacings obtained by Esser, Eilender, and Bungardt (1938)[51] to the melting temperature gives $d_{\text{nn}} = 2.55\,\text{Å}$ for pure Ni at $T_m^o = 1728\,\text{K}$. This value of d_{nn}, together with the critical value $\langle\mu^2\rangle_{\text{Thermal}}$ at T_m^o, leads to $\delta_{\text{Critical}} = 0.114$ in the harmonic or $\delta_{\text{Critical}} = 0.149$ for the anharmonic case using extrapolated empirical data. Based on this analysis, the empirically determined δ_{Critical} of 0.115 ± 0.01 for the onset of boron implantation-induced amorphization of Ni is, within experimental error, in quite good agreement with the δ_{Critical} values for the onset of heat-induced melting. This agreement is the first direct confirmation of the generalized Lindemann melting hypothesis for solid-state c-a transformation phenomena.

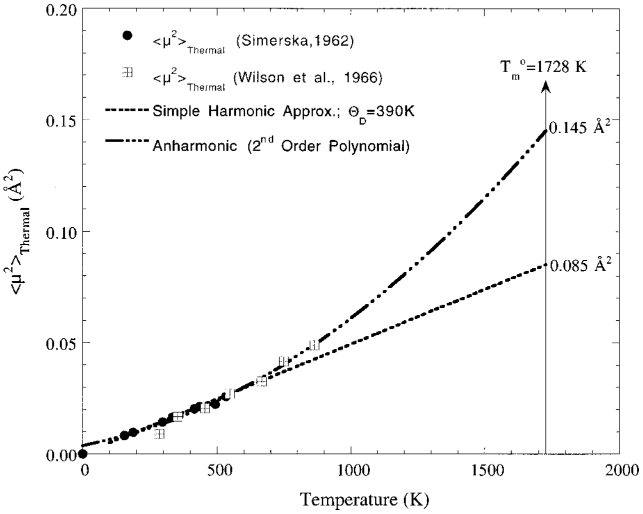

FIG. 10. The temperature dependence of $\langle\mu^2\rangle_{\text{Thermal}}$ determined using x-ray diffraction results from Simerská's (1962) (Ref. 49) and Wilson *et al.*'s (1966) (Ref. 50) works. Also shown are δ_{Critical} values obtained by the linear (harmonic) and the quadratic (anharmonic) extrapolations to Ni's melting point.

B. Compositional dependence of static MSD $\langle\mu^2\rangle_{\mathrm{Static}}$

In Fig. 9 the empirically measured $\langle\mu^2\rangle_{\mathrm{Static}}$ is seen to increase approximately parabolically with boron concentration x, with a gradual upward-concaving trend starting at 7 $\sim$8 at. % boron. This result seems to contradict the expectation that $\langle\mu^2\rangle_{\mathrm{Static}}$ should possess a downward-concaving parabolic dependence on the solute concentration x because of its direct proportionality to $x\cdot(1-x)$ term.[14] The compositional dependence of $\langle\mu^2\rangle_{\mathrm{Static}}$ obtained from Linker's experimental studies on the amorphization of niobium films by boron implantation appeared to agree with the $x\cdot(1-x)$ parabolic dependence;[35] furthermore, his data suggested that the maximum in the $\langle\mu^2\rangle_{\mathrm{Static}}$ coincides with the peak of the lattice parameter dilatation. By contrast, our results shown in Fig. 9 indicate that the maximum in $\langle\mu^2\rangle_{\mathrm{Static}}$ is not achieved at the peak of the lattice-parameter dilatation, but rather delayed until near the completion of the c-a transition process.

These apparent inconsistencies can be resolved by examining the compositional dependence of $\langle\mu^2\rangle_{\mathrm{Static}}$. For binary cubic alloys, Shirley and Fisher[14] have derived the following expressions for $\langle\mu^2\rangle_{\mathrm{Static}}$:

$$\langle\mu^2\rangle_{\mathrm{Static}}=0.385x(1-x)\gamma^2a^2(1+5.93\alpha_1+1.74\alpha_2+4.53\alpha_3+\cdots)\ \ (\mathrm{fcc}),\tag{12a}$$

$$\langle\mu^2\rangle_{\mathrm{Static}}=2.836x(1-x)\gamma^2a^2(1+0.75\alpha_1+0.50\alpha_2-0.86\alpha_3+\cdots)\ \ (\mathrm{bcc}),\tag{12b}$$

where x denotes the solute concentration, a is the lattice parameter, α_i's are the Cowley-Warren short-range-order parameters, and $\gamma=d\ln a/dx=(da/a)/dx$ provides a measure of the composition dependence on the atomic size mismatch. In Fig. 11 we have illustrated how the atomic size mismatch term γ^2 can dramatically alter the composition dependence of $\langle\mu^2\rangle_{\mathrm{Static}}$. For a complete solid solution or alloy with large solubility limits where atomic size mismatch is small, $\langle\mu^2\rangle_{\mathrm{Static}}$ would vary with x in the form given by the product $x\cdot(1-x)$, with the peak of the parabolic curve centered on $x=0.5$ and crossing the x axis at $x=0$ and $x=1$ (top diagram). However, for cases similar to Ni-B system where the solubility of B in Ni is severely limited, the rate of the lattice-parameter change with x can lead to a significant departure of $\langle\mu^2\rangle_{\mathrm{Static}}$ from the $x\cdot(1-x)$ dependence. A hypothetical parabolic dependence of lattice parameter a on solute concentration x, incorporating the dilatation magnitude and Δx range similar to the results shown in Fig. 6, has been constructed to illustrate the effect of various parameter changes. As shown in Fig. 11, the presence of a maximum (or minimum) in lattice parameter means the slope da/dx would go to zero, causing the product $x(1-x)\gamma^2$ to exhibit a minimum at the respective lattice-parameter peak position. The rate of the lattice-parameter change with composition, with respect to $x\cdot(1-x)$'s peak position, then determines the relative magnitudes of the resulting $\langle\mu^2\rangle_{\mathrm{Static}}$ curves. A shift in the lattice parameter maximum from $x=0.5$ to $x=0.8$ with the same Δx range results in a $\langle\mu^2\rangle_{\mathrm{Static}}$ curve dominated by a large parabolic curve below $x=0.8$, as the product of $x\cdot(1-x)$ and $(da/dx)^2$ peaks before the lattice parameter maximum. For the same reason a large parabolic curve beyond $x=0.2$ would dominate the resulting $\langle\mu^2\rangle_{\mathrm{Static}}$ curves if the lattice-parameter maximum is shifted from $x=0.5$ to $x=0.2$. In contrast to γ^2, the variation of the lattice parameter a^2 term is so small that its effects on $\langle\mu^2\rangle_{\mathrm{Static}}$ magnitude can be approximated by a scaling constant. The Cowley-Warren short-range-order parameter, defined as $\alpha_i=1-p_B(r_i)/x_B(r_i)$ where $p_B(r_i)$ is the probability of finding a B atom as a r_i neighbor of an A atom, will be negative if there is a greater tendency for short-range ordering or positive if there is a greater tendency for clustering of like atoms.[28] Studies done using complete solid solutions[52] suggest the maximum amplitude of $|\alpha_1|$ for the nearest-neighbor shell is about 0.10$\sim$0.16, which is much less than 1 and thus likely to be overwhelmed by the effect of the γ^2 term. Hence for a binary solid solution with large atomic size mismatch among its constituent elements, the effect of the γ^2 term must be considered along with $x\cdot(1-x)$ when determining the composition dependence of $\langle\mu^2\rangle_{\mathrm{Static}}$.

In Fig. 12 we have plotted $\gamma=d\ln a/dx$ and the product $x(1-x)\gamma^2$ as a function of x for Ni-B system based on a second-order polynomial fit to the empirical composition dependence of lattice parameter shown in Fig. 6. The minimum in γ^2 occurred at $x=0.05$ where $d\ln a/dx$ equals zero, hence a sharp increase in the product $x(1-x)\gamma^2$ did not begin until the implanted B concentration exceeded 5 at. %. The experimentally observed upward-concaving $\langle\mu^2\rangle_{\mathrm{Static}}$ trend actually reflects the effect of a $x(1-x)\gamma^2$ minimum occurring near the B concentration where the lattice-parameter maximum is attained. This result, the minimum of $\langle\mu^2\rangle_{\mathrm{Static}}$ occurs when the change in lattice parameter reaches a maximum (or minimum), is in direct contrast to the previous assertion made by Linker.[35] Whereas Linker's data suggested a maximum in $\langle\mu^2\rangle_{\mathrm{Static}}$ occurring near the lattice-parameter maximum, we believe it is the maximum $\langle\mu^2\rangle_{\mathrm{Static}}$ value prior to the completion of the c-a transformation that should be used for the evaluation of the critical Lindemann parameter $\delta_{\mathrm{Critical}}$. This is because the damage induced is statistically distributed throughout the lattice, so that when making experimental measurement of $\langle\mu^2\rangle_{\mathrm{Static}}$ from the Bragg reflections, what is being measured is only the average from those crystals which still do not possess the necessary $\langle\mu^2\rangle_{\mathrm{Critical}}$ for amorphization. It is only near the completion of the c-a transformation that the average $\langle\mu^2\rangle_{\mathrm{Static}}$ value of the crystalline remnants approaches the actual $\langle\mu^2\rangle_{\mathrm{Critical}}$ value needed for the onset of the amorphization.

VII. POLYMORPHOUS MELTING T_o CURVE

Equations (3a) and (3b) can be used to construct a polymorphous melting T_o curve for the Ni-B system using the values of $\delta_{\mathrm{Critical}}$ and compositional dependence of $\langle\mu^2\rangle_{\mathrm{Static}}$ determined from this work, together with the following relationships:[53]

$$M=(1-x)M_{\mathrm{Ni}}+(x)M_{\mathrm{B}},$$

$$\frac{1}{\theta_o^2}=\frac{(1-x)}{\theta_{\mathrm{Ni}}^2}+\frac{(x)}{\theta_{\mathrm{B}}^2},$$

$$d_{\mathrm{nn}}=(1-x)d_{\mathrm{nn,Ni}}+(x)d_{\mathrm{nn,B}},\tag{13}$$

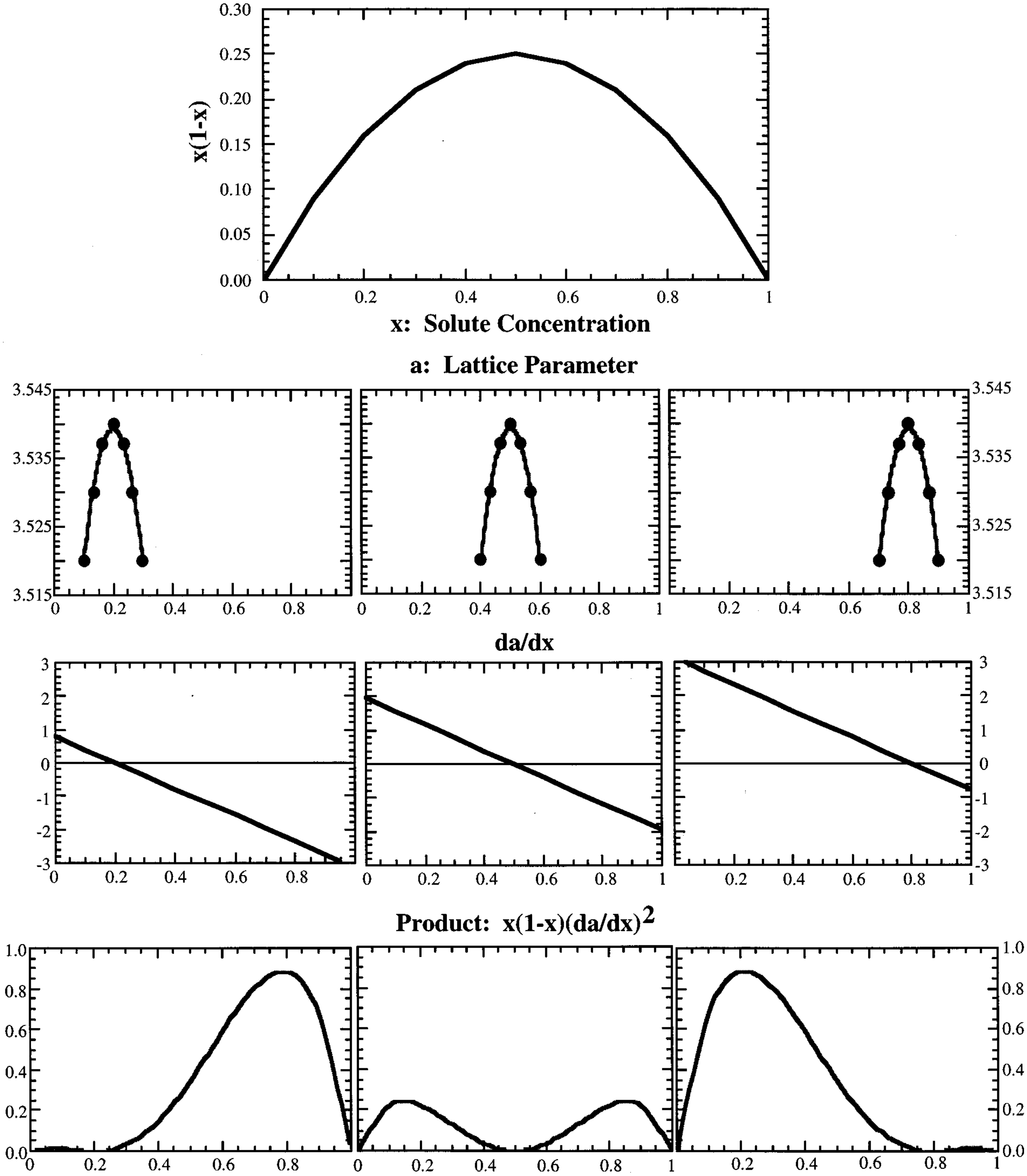

FIG. 11. A graphical illustration of the effect of $x(1-x)$ and $\gamma = 1/a(da/dx)$ on the compositional dependence of $\langle\mu^2\rangle_{\mathrm{Static}}$ described in Eq. (12). The top diagram shows the basic functional form of $x(1-x)$ versus the solute concentration x. The diagrams (in each column) below shows how the difference in the position of lattice parameter peak affects the form of the product $x(1-x)(da/dx)^2$ via the corresponding changes in (da/dx).

where x denotes the atomic concentration of boron. It is important to recognize that the calculated T_o curve based on Eqs. (3a), (3b) and (13) contain several simplifying assumptions. First, the anharmonic effect for the temperature dependence of $\langle\mu^2\rangle_{\mathrm{Thermal}}$ is not taken into account, and second, θ_o and d_{nn} are assumed to be temperature independent. Ignoring the anharmonic dependence of $\langle\mu^2\rangle_{\mathrm{Thermal}}$ on temperature is expected to lead to an underestimate of the rate of change of T_m^d with $\langle\mu^2\rangle_{\mathrm{Static}}$ in the high-temperature regime. The error due to the negligence of the thermal expansion of d_{nn} for Ni and B is estimated to be less than 2% for temperatures up to $T_f(\mathrm{Ni}) = 1728\,\mathrm{K}$.[47] Krivoglaz (1969) has calculated Debye temperatures for Al and Cu based on a semiphenomenological vibration model, and concluded that θ_o for fcc lattices is only weakly dependent on the temperature.[15] The variation of $\langle\mu^2\rangle_{\mathrm{Static}}$ with boron concentration was obtained directly from the modified Wilson plot analysis, while the values of $\langle\mu^2\rangle_{\mathrm{Critical}}$ and $\delta_{\mathrm{Critical}}$ were taken from the experiment for the onset of solid-state c-a transition. The nearest-neighbor distance for Ni and B were set to a value averaged over the

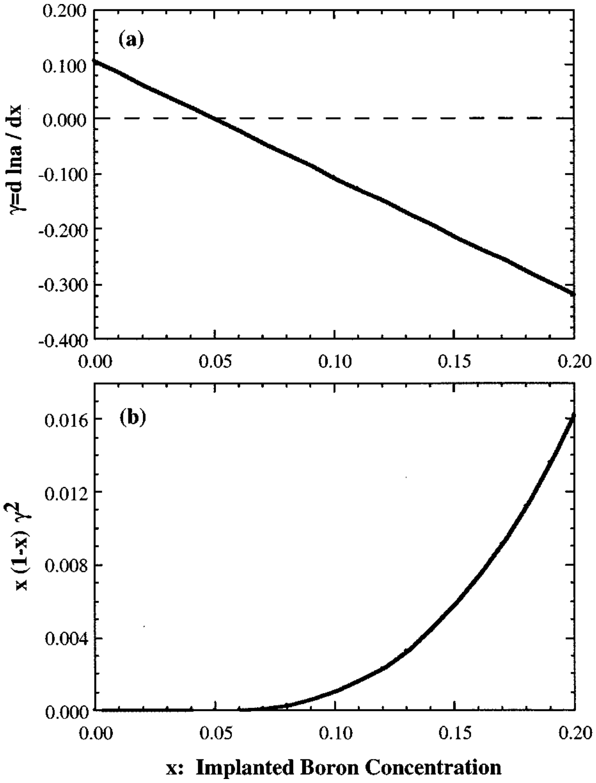

FIG. 12. The compositional dependence of $\langle\mu^2\rangle_{\rm Static}$ predicted using Eq. (12) with the empirically measured lattice-parameter change obtained from Ni-B system (Fig. 6): (a) a plot of the empirical compositional dependence of γ for Ni-B solid solution; (b) the theoretical $\langle\mu^2\rangle_{\rm Static}$ relation with the boron concentration x given by $x(1-x)\gamma^2$.

applicable temperature range, giving $d_{\rm nn}({\rm Ni})=2.5139\,$Å and $d_{\rm nn}({\rm B})=1.9060\,$Å, respectively.[47] The Debye temperatures for the constituent elements were chosen based on the criterion of best-fit results to the respective T_m^o from among reported θ_o range; this gives $\theta_o({\rm Ni})=390\,{\rm K}$ (reported θ_o ranging from 375~476 K) and $\theta_o({\rm B})=1365\,{\rm K}$ (reported θ_o ranging from 1250~1480 K).[46]

In Fig. 13, the T_o curve calculated using GLMC from the available experimental data has been superimposed on the Ni-B equilibrium phase diagram[54] with a solid line drawn to serve as a guide. The initial decrease in T_m^d follows the liquidus curve fairly closely but drops abruptly as the boron concentration approaches ~10 at. %. This sharp plunge in T_m^d is due to the inherent constraints imposed by the GLMC that $\langle\mu^2\rangle_{\rm Static}$ cannot exceed $\langle\mu^2\rangle_{\rm Critical}$ obtained for the onset of melting/amorphization. The qualitative features of the T_o curve constructed using the semiempirical GLMC is consistent with the thermodynamics-based theoretical predictions. Using the equality condition of Gibbs free energies for the partitionless melting and assuming no equilibrium phase separation, Fecht, Desré, and Johnson have derived a differential form of the generalized Clapeyron relation that defines the polymorphous melting surface $T_o(P,C)$ for a metastable binary solid solution as a function of composition C and pressure P:[12]

$$(\partial T_m/\partial C)_P=-A_m/\Delta S_m \quad \text{(isobaric partitionless melting)}, \tag{14a}$$

$$(\partial P_m/\partial C)_T=A_m/\Delta V_m \quad \text{(isothermal partitionless melting)}, \tag{14b}$$

$$(\partial P_m/\partial T)_C=\Delta S_m/\Delta V_m \quad \text{(isoconcentration partitionless melting)}, \tag{14c}$$

where P_m is the melting pressure, ΔS_m and ΔV_m are the entropy and volume change upon melting, and A_m, termed ‘‘partitionless melting state affinity,’’ is a function of the chemical potential of A and B constituents in the liquid and crystalline states. If the constituents A and B in the binary solid solution with negative enthalpy of mixing have different crystal structures, A_m cannot be zero and must increase with decreasing temperature. Together with Kauzmann's criterion that a supercooled liquid must undergo thermodynamic transition to the ideal glass at T_K to avoid having the entropy of the supercooled liquid lower than that of the crystalline phase,[11] Eq. (14a) shows that the melting temperature of Ni-B solid solution as a function of solute concentration will plunge sharply with a slope equal to $-A_m/\Delta S_m$ and, beyond the triple point T_K where $\Delta S_m=\Delta G_m=\Delta H_m=0$, the T_o curve will drop abruptly to zero. This sharp plunging of T_o curve at the thermodynamic metastability limit of the crystal (represented by T_K) is the key feature of the T_o curve based on GLMC. Instead of relying on the extrapolated thermodynamic data of supercooled liquid for temperatures below the melting point, GLMC uses the more accessible $\langle\mu^2\rangle_{\rm Static}$ and $\langle\mu^2\rangle_{\rm Critical}$ to provide a measure for the thermodynamic stability of the metastable solid solution, thus providing a more reliable and self-consistent means of extending the T_o curve below the eutectic temperature.

The T_o curve also provides an alternative verification for GLMC through the determination of the critical composition C^* at which $T_m^d=T_K$. Within the framework of GLMC, C^* represents the minimum solute concentration required to melt (or amorphize) the crystal, thus defining the limits of the ‘‘glass formation range’’ (GFR). It is important to compare the value of C^* determined by GLMC with that predicted by the mechanical instability criterion for amorphization proposed by Egami and Waseda.[7] Based on their analyses of the local strain effects arising from the difference in atomic sizes of solvent (B) and solute (A) atoms, the minimum solute concentration $C_A^{\rm Min}$ necessary for glass formation by rapid quenching from melt is given by[7]

$$C_A^{\rm Min}\cong 0.10\frac{\Omega_B}{|\Delta\Omega|}=0.10\frac{R_B^3}{|R_B^3-R_A^3|}, \tag{15a}$$

where $|\Delta\Omega|$ denotes the absolute difference in the atomic volumes of the constituent elements, and Ω and R are the atomic volume and radii of A and B atoms, respectively. More recently, Egami (1997) suggested for solid-state amorphization the composition limits of the amorphous phase formation should be modified as[55]

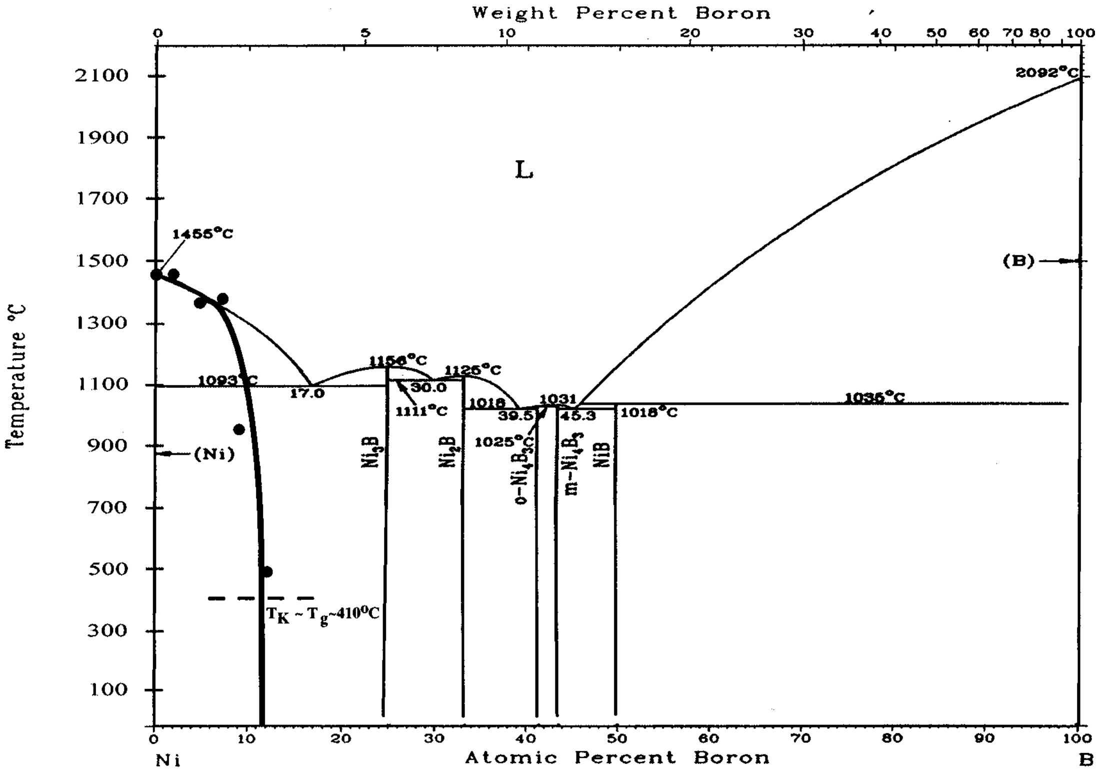

FIG. 13. T_o curve obtained using GLMC for the Ni-rich side of B-Ni binary phase diagram. The position of the T_o curve is calculated using empirically determined compositional dependence of $\langle\mu^2\rangle_{\mathrm{Static}}$. The glass transition temperature $T_K \sim T_g$ is taken as roughly one-half of the eutectic temperature (Ref. 57). The critical solute concentration as given by the intersection of T_o and T_k curves is estimated to be 0.10 ± 0.02.

$$C_A^{\mathrm{Min}}=0.25\frac{\Omega_B}{|\Delta\Omega|}=0.25\frac{R_B^3}{|R_B^3-R_A^3|}. \tag{15b}$$

Using the atomic radii of $B=0.920$ Å and $Ni=1.246$ Å,[47] the minimum B solute concentration for glass formation via rapid quenching would be 16.7 at. %, whereas for solid-state amorphization the minimum B solute concentration required would be 27.9 at. % (with composition limit extrapolated to $T=300\,°C$). In contrast, the steeply plunging T_o curve based on GLMC predicts 10 ± 2 at. % to be the minimum B solute concentration needed to induce solid-state c-a transition in Ni crystal. It is evident that the actual position of T_K will not affect this estimate of C^* since T_o curve is almost vertical for $T_m^d < \frac{2}{3}T_m^o$. Moreover, this value of 10 at. % B for the onset of c-a transformation in Ni-B system is consistent with that derived from the statistical analyses of amorphous phase volume fractions, namely $C_c=8.7$ at. % for the current experiment and $C_c=9.3$ at. % from the RBS/channeling results.[34] The agreement between the kinetically determined values of C_c and the value of C^* predicted by the T_o curve provides further validation of the GLMC. The somewhat higher critical solute concentration predicted by the Egami-Waseda criterion is consistent with the fact that the criterion is based on the topological mechanical instability of the crystalline phase. In contrast, GLMC is based on a thermodynamic criterion for melting and thus requires a smaller solute concentration for amorphization. The agreement between experimentally determined C_c and that predicted by T_o curve (C^*) also indicates that it is the implanted solute, rather than radiation damage, that is the primary cause for the instability of the crystal during the ion-implantation process. This conclusion is consistent with the empirical findings that there appears to be no strong ion-mass dependence of critical dose for implantation induced amorphization, as well as the observations that self-ions and noble-gas implantations into metals do not result in amorphous phase formation.[56]

VIII. CONCLUSIONS

The objective of this study is to assess the hypothesis of solid-state amorphization as an extension of thermodynamic melting within the framework provided by the generalized Lindemann melting criterion. A natural consequence of the GLMC approach has been the selection of the Lindemann parameter, $\delta=\sqrt{\langle\mu^2\rangle_{\mathrm{Total}}}/d_{\mathrm{nn}}$, as a universal disorder parameter whose magnitude is linearly related to the direct summation of thermal and static mean-square displacements in the respective transition process. Boron-implantation induced amorphization of polycrystalline nickel at 77 K constitutes an effective way of ''melting'' the nickel solid solution by supersaturating the crystal with solute atoms while avoiding equilibrium phase separation. It is found empirically that the critical Lindemann parameter $\delta_{\mathrm{Critical}}$ for the crystal at the onset of amorphization agrees, within experimental error, to that for the onset of melting. This is the first direct confirmation for the generalized Lindemann melting hypothesis, suggesting that the conditions governing the destabilization during the thermodynamic melting should be equally applicable to the solid-state c-a transition. A polymorphous T_o curve has been constructed based on the GLMC using the empirical relation found between the static disorder introduced into the crystal and the implanted boron concentration. The statistical analyses of the amorphous volume fraction yield a critical solute concentration value consistent with the prediction of the T_o curve, further underscoring the notion that ion-implantation-induced amorphization is simply the polymorphous melting of a defective crystal below the ideal glass transition temperature.

ACKNOWLEDGMENTS

The authors would like thank P. Baldo, L. Funk, and A. McCormick for their assistance with the ion-implantation experiments and the determination of boron concentration. Special thanks are extended to L. E. Rehn for his helpful insights and support in using ion accelerator facility. This work was supported by the U.S. Department of Energy, Basic Energy Sciences-Materials Sciences, under Contract No. W-31-109-Eng-38.

---

*Author to whom correspondence should be addressed. Present address: Argonne National Laboratory, Materials Science Division, Argonne, IL 60439.

[1] W. L. Johnson, Prog. Mater. Sci. **30**, 81 (1987).

[2] P. R. Okamoto, N. Q. Lam, and L. E. Rehn, in *Solid State Physics*, edited by H. Ehrenreich and F. Spaepen (Academic, Boston, 1999), Vol. 52, p. 1.

[3] L. E. Rehn, P. R. Okamoto, J. Pearson, R. Bhadra, and M. Grimsditch, Phys. Rev. Lett. **59**, 2987 (1987).

[4] P. R. Okamoto, L. E. Rehn, J. Pearson, R. Bhadra, and M. Grimsditch, J. Less-Common Met. **140**, 231 (1988).

[5] P. R. Okamoto and M. Meshii, in *Science of Advanced Materials*, edited by H. Wiedersich and M. Meshii (ASM International, Materials Park, OH, 1990), p. 33.

[6] D. Wolf, P. R. Okamoto, S. Yip, J. F. Lutsko, and M. Kluge, J. Mater. Res. **5**, 286 (1990).

[7] T. Egami and Y. Waseda, J. Non-Cryst. Solids **64**, 113 (1984).

[8] T. Egami, K. Maeda, and V. Vitek, Philos. Mag. A **41**, 883 (1980).

[9] T. Egami and D. Srolovitz, J. Phys. F **12**, 2141 (1982).

[10] F. A. Lindemann, Phys. Z. **11**, 609 (1910).

[11] W. Kauzmann, Chem. Rev. **43**, 219 (1948).

[12] H. J. Fecht, P. J. Desré, and W. L. Johnson, Philos. Mag. B **59**, 577 (1989).

[13] A. L. Greer, J. Less-Common Met. **140**, 327 (1988).

[14] C. G. Shirley and R. M. Fisher, Philos. Mag. A **39**, 91 (1979).

[15] M. A. Krivoglaz, *Theory of X-ray and Thermal Neutron Scattering by Real Crystals* (Plenum, New York, 1969).

[16] J. A. Eastman and M. R. Fitzsimmons, J. Appl. Phys. **77**, 522 (1995).

[17] A. Voronel and S. Rabinovich, J. Phys. F **17**, L193 (1987).

[18] C. E. Krill, III, J. Li, C. M. Garland, C. Ettl, K. Samwer, and W. L. Johnson, J. Mater. Res. **10**, 280 (1995).

[19] M. Born, J. Chem. Phys. **7**, 591 (1939).

[20] J. J. Gilvarry, Phys. Rev. **102**, 308 (1956).

[21] A. P. Malozemoff, in *Glassy Metals I: Ionic Structure, Electronic Transport, and Crystallization*, edited by H.-J. Güntherodt and H. Beck (Springer, New York, 1981), Vol. 46, p. 79.

[22] L. Cartz, Proc. Phys. Soc. London, Sect. B **68**, 957 (1955).

[23] S.-A. Cho, J. Phys. F **12**, 1069 (1982).

[24] J. N. Shapiro, Phys. Rev. B **1**, 3982 (1970).

[25] R. P. Gupta and P. K. Sharma, J. Chem. Phys. **48**, 2451 (1968).

[26] A. K. Singh and P. K. Sharma, Can. J. Phys. **46**, 1677 (1968).

[27] P. C. Liu, N. J. Zaluzec, P. R. Okamoto, and M. Meshii, in *Proceedings of Microscopy and Microanalysis 1996*, edited by G. W. Bailey, J. M. Corbett, R. V. W. Dimlich, J. R. Michael, and N. J. Zaluzec (San Francisco Press, Inc., Minneapolis, MN, 1996), p. 990.

[28] B. E. Warren, *X-ray Diffraction* (Dover, New York, 1990).

[29] Powder Diffraction Files, JCPDS-International Center for Diffraction Data, Swarthmore, PA, PDE No. 04-0850, 1953 (unpublished).

[30] J. F. Ziegler, J. P. Biersack, and U. Littmark, *The Stopping and Range of Ions in Solids* (Pergamon, New York, 1985).

[31] R. F. Egerton, *Electron Energy-Loss Spectroscopy in the Electron Microscope* (Plenum, New York, 1986).

[32] M. Vollmer, J. D. Meyer, R. W. Michelmann, and K. Bethge, Nucl. Instrum. Methods Phys. Res. B **117**, 21 (1996).

[33] S. Swaminathan, I. P. Jones, N. J. Zaluzec, D. M. Maher, and H. L. Fraser, Mater. Sci. Eng., A **170**, 227 (1993).

[34] A. V. Drigo, M. Berti, A. Benyagoub, H. Bernas, J. C. Pivin, F. Pons, L. Thomé, and C. Cohen, Nucl. Instrum. Methods Phys. Res. B **19/20**, 533 (1987).

[35] G. Linker, Mater. Sci. Eng., A **69**, 105 (1985).

[36] G. Linker, Nucl. Instrum. Methods Phys. Res. B **19/20**, 526 (1987).

[37] L. Reimer, *Transmission Electron Microscopy—Physics of Image Formation and Microanalysis* (Springer, New York, 1989).

[38] M. Blackman, Proc. R. Soc. London, Ser. A **173**, 68 (1939).

[39] B. K. Vainshtein, Dokl. Akad. Nauk SSSR **104**, 537 (1955).

[40] J. Gjønnes, Acta Crystallogr. **12**, 976 (1959).

[41] F. Paasche, H. Olbrich, U. Schestag, P. Lamparter, and S. Steeb, Z. Naturforsch. **37A**, 1139 (1982).

[42] J. Ankele, J. Mayer, P. Lamparter, and S. Steeb, Z. Naturforsch., A: Phys. Sci. **49**, 771 (1994).

[43] G. Grimvall, *Thermophysical Properties of Materials* (North-Holland, Amsterdam, 1986).

[44] N. Q. Lam and P. R. Okamoto, MRS Bull. **19**, 41 (1994).

[45] R. W. James, *The Optical Principles of the Diffraction of X-rays* (Cornell University Press, New York, 1965).

[46] C. H. MacGillavry and G. D. Rieck, in *The International Union of Crystallography*, edited by K. Lonsdale (Kluwer Academic, Boston, 1992), Vol. III.

[47] W. B. Pearson, *A Handbook of Lattice Spacings and Structures of Metals and Alloys* (Pergamon, New York, 1967).

[48] M. O. Robbins, G. S. Grest, and K. Kremer, Phys. Rev. B **42**, 5579 (1990).

[49] M. Simerská, Czech. J. Phys., Sect. B **12**, 858 (1962).

[50] R. H. Wilson, E. F. Skelton, and J. L. Katz, Acta Crystallogr. **21**, 635 (1966).

[51] H. Esser, W. Eilender, and K. Bungardt, Arch. Eisenhuettenwese **12**, 157 (1938).

[52] B. L. Averbach, *Theory of Alloy Phases* (American Society for Metals, Cleveland, 1956), p. 301.

[53] S. Rabinovich, A. Voronel, and L. Peretzman, J. Phys. C **21**, 5943 (1988).

[54] T. B. Massalski, H. Okamoto, P. R. Subramanian, and L. Kacprzak, in *Binary Alloy Phase Diagrams*, edited by T. B. Massalski (ASM International, Materials Park, OH, 1990), Vol. 1.

[55] T. Egami, Mater. Sci. Eng., A **226–228**, 261 (1997).

[56] B. Rauschenbach and V. Heera, Zentralinstitut für Kernforschung Rossendorf, Dresden, Report No. ZfK-630, 1988 (unpublished).

[57] L. Battezzati, Philos. Mag. B **61**, 511 (1990).